Journal of Materials Research and Technology 32 (2024) 395–409

Contents lists available at ScienceDirect

Journal of Materials Research and Technology

journal homepage: www.elsevier.com/locate/jmrt

Comprehensive evaluation of CFRP laminates using NDT methods for aircraft applications

Muhammad Akhsin Muflikhun [a,*], Bodo Fiedler [b]

[a] Mechanical and Industrial Engineering Department, Gadjah Mada University, Indonesia
[b] Institute of Composite and Polymer, Hamburg Institute of Technology, Germany

A R T I C L E I N F O

Handling editor: SN Monteiro

Keywords:
Non-destructive testing
CFRP laminates
Failure analysis
Crack propagation
DCB test

A B S T R A C T

The evaluation of carbon fiber reinforced polymers (CFRP) laminates during and after the Mode I test was successfully conducted, integrating non-destructive testing of acoustic emission (AE) and ultrasound scanning. Two different specimens $[+45°/-45°/0°]_{2S}$ and $[0°/+45°/-45°]_{2S}$ were used to detect the effects of stacking sequences of the laminates. Results indicated that applying AE sensors to the specimens slightly affect to the laminate performance. Thus, the laminates are validated and showed that for $[+45°/-45°/0°]_{2S}$ laminates, the system can withstand load and increase the displacement at break more than twice of $[0°/+45°/-45°]_{2S}$ laminates. Moreover, the ultrasound scanning showed that the crack trace is visible. $[+45°/-45°/0°]_{2S}$ laminates have smaller crack around 24 mm compared to $[0°/+45°/-45°]_{2S}$ laminates with 30 mm. Image analysis revealed that after specimen are forced to open, the $[+45°/-45°/0°]_{2S}$ laminates can prevent long crack compared to $[0°/+45°/-45°]_{2S}$ laminates. The double cantilever beam (DCB) test, employing various stacking sequences, demonstrated excellent examination results using non-destructive testing. Theoretical calculations regarding residual thermal expansion due to different coefficients of thermal expansion also revealed a slight impact of varying manufacturing temperatures on the laminates. These findings offer valuable insights for detecting, predicting, and preventing specimen failures in aircraft and aerospace structures without resorting to destructive examinations, facilitating appropriate preventive maintenance.

1. Introduction

Composite laminates consisting of carbon fiber reinforced polymers (CFRP) have garnered significant interest among engineers for use in various applications, including structures [1], aircraft [2], spacecraft [3], buildings [4], automotive [5], and medical [6]. The excellent performance of CFRP, whether used in pure CFRP laminates or combined with other materials, has made it one of the most adaptable styles of CFRP laminates. Combining CFRP with materials such as steel plate cold commercial (SPPC), Al, Ti, wood, or nanomaterials has shown that the performance of CFRP can exceed expectations [7–10]. The composition of basic CFRP laminates is relatively simple compared to other structures, such as metal alloys. It consists of matrix, bonding elements, and carbon fiber as the strengthening element are combined layer by layer. The uniqueness of CFRP also lies in the strength capability of the laminates, which can be adjusted using a simple stacking sequences model that is widely applied. By changing the angle of the fiber in one layer, the strength can be altered. Thus, CFRP laminates have become well-known for their application in modern aircraft structures. The Boeing 787 Dreamliner, Airbus A350, A350 XWB, and Boeing AH-66 are examples of models that use CFRP as parts of the composite structures, accounting for more than 50% of the weight [11,12].

The wide range of applications mentioned in many published papers [13–16] has drawn attention to CFRP structures from both manufacturers and maintenance personnel. Because of these structures rely on bonding between layers, crack detection, early preliminary failure detection, and repair processes and strategies have garnered significant attention from researchers. It is not economically feasible to apply conventional models that rely on destructive basic inspection related to checking and maintaining CFRP laminates. Therefore, several engineers and researchers develop different techniques to detect and determine the condition of laminates using non-destructive testing (NDT). Tao et al. [13] identified the composite based on glass fibers laminates using digital shearography combined with thermal loading system. The novel study of it occurred for the thick laminates applications where the instrument was perfectly used in marine structures that used thick

---

* Corresponding author.
E-mail address: akhsin.muflikhun@ugm.ac.id (M.A. Muflikhun).

https://doi.org/10.1016/j.jmrt.2024.07.196
Received 29 March 2024; Received in revised form 22 July 2024; Accepted 24 July 2024

laminates. Hence, in thin laminates, further study needs to be further investigated as well as in carbon fiber system. More comprehensive monitoring of composite laminates reported by Wang et al. [17] using acoustic emission (AE) and digital image correlation (DIC) techniques. The study was introduced the NDT evaluation to be applied in fatigue tests. Another breakthrough of the study occurred based on the tools that used in the study which are combining principal component analysis (PCA) and K-means++ algorithms. The damage model also incorporated with cumulative damage index (CDI). The results showed that AE have more advantages compared to DIC in term of real time evaluation. However, the study only used limited variation of the stacking sequences in their work.

The combination of NDT and destructive test was introduced by Gowelski et al. [18] using operational deflection shapes (ODS). DIC, and tensile loading. The aging scenario of CFRP laminates also induced of their study. The results showed that high temperature exposure significantly decrease the strength and young modulus of the laminates. In addition, Mirzaei and Shokrieh [19] used the thermal manipulation of the laminates in their study couple with the fatigue test. The study was incorporated with finite element model (FEM) using temperature-damage evolution (TDE) model. In addition, Yang et al. [20] investigates CFRP laminates using ultrasonic tomography. The study also used a model called Gabor filter with information diagram (GF-ID). The results showed that using NDT model with GF-ID give higher performance compared with classical random transform model.

There are still many study that used different NDT model applied in different scenario of the composite laminates. Many of them showed that the NDT technique can be used online during testing process, or after testing process without doing destructive assessment into the samples. Since the method was introduced, the comparison or combination of the methods was introduced among the studies such as impulse excitation technique, convolution neural network (CNN), step heating thermography (SHT), three-dimensional (3D) photothermal analysis, induction thermography, and thermoelastic stress analysis (TSA) [21–28].

Among the different techniques introduced by researchers to evaluate CFRP laminates, comprehensive analysis using AE and ultrasound analysis for Mode I fracture toughness or double cantilever beam (DCB) test of CFRP laminates has been reported [17,29] in only a few studies based on the literature review that showed in the current section. Although several works existed using DCB, or mixed-mode bending (MMB) method to evaluate Mode I [30,31], the combination of AE, and ultrasound analysis is not much occurred. In term of It is also shown that the combination of NDT analysis and incorporated with theoretical calculation of thermal effect during manufacturing process related to the different stacking sequences of CFRP laminates have not been applied in previous works, especially in terms of Mode I analysis. Therefore, these gaps became the novelty of the present paper, where the analysis related to the different stacking sequences of thin CFRP laminates characterized using the ISO 15024 standard [32] test for the first time is introduced. The NDT techniques used were AE and ultrasound analysis combined. The results are an important aspect to be used in thin CFRP laminates applied in aerospace and spacecraft structures, where it is difficult to use destructive techniques to observe the quality of the laminates.

2. Materials and methods

2.1. Materials

Unidirectional carbon fiber prepreg from Hexcel namely HexPly M21/34%/UD194/T800S–24K/600HLU (resin/resin content (%)/fiber weight (gsm)/fiber type -unidirectional-) was used in the present paper. The characteristic of the prepreg can be seen in Table 1. Samples were prepared by using autoclave method where the sequences were set to $[+45^\circ/-45^\circ/0^\circ]_{2S}$ ($[+45^\circ/-45^\circ/0^\circ/0^\circ/-45^\circ/+45^\circ/+45^\circ/-45^\circ/0^\circ/0^\circ/-45^\circ/+45^\circ]$) and $[0^\circ/+45^\circ/-45^\circ]_{2S}$ ($[0^\circ/+45^\circ/-45^\circ/-45^\circ/+45^\circ/0^\circ/0^\circ/+45^\circ/-45^\circ/-45^\circ/+45^\circ/0^\circ]$). The autoclave process was performed at 180 °C, held for 4 h at a pressure of 7 Bar, with a room temperature (RT) of 25 °C. Based on the tension testing, the elastic modulus of $[0^\circ/+45^\circ/-45^\circ]_{2S}$ laminate was 61.49 GPa and $[+45^\circ/-45^\circ/0^\circ]_{2S}$ laminate was 60.47 GPa. The Ultimate tensile stress of $[0^\circ/+45^\circ/-45^\circ]_{2S}$ laminate was 1123.97 MPa and $[+45^\circ/-45^\circ/0^\circ]_{2S}$ laminate was slightly higher with 1227.95 MPa. For the DCB test, polytetrafluoroethylene (PTFE) thin film was inserted into the one edge of the sample that act as the crack enclosure. After cured, specimen was prepared to cut based on the ISO 15024 [32]. To ensure the cutting precision, samples were cut using ATM Brillant 220. The loading block with the size of 20 mm cube size was used. The dimension of the specimen can be seen in Fig. 1.

Table 1
Materials properties [30,33–35].

Properties	Units	Value
Prepreg mass (cured)	g/cm^2	294
Fiber volume fraction	%	59.2
Glass Transition Temp.	°C	195
Autoclave time	h	4
Autoclave temp.	°C	180
Autoclave press.	bar	7
Longitudinal modulus (E_1)	GPa	130.7
Transverse modulus (E_2)	GPa	8.01
Poisson's ratio (ϵ_{12})	–	0.35
Shear modulus (G_{12})	GPa	5.31
Transverse tensile strength (Y^T)	MPa	40.5
Shear strength (S^L)	MPa	69.6
Tension Strength (ASTM D3039)	MPa	2860
Tension Modulus (ASTM D3039)	GPa	160
Compression Strength (ASTM D695)	MPa	1790
Compression Modulus (ASTM D695)	GPa	148
ILSS (ASTM D2344)	MPa	110
Longitudinal CTE α	°C^{-1}	−5.02E-07
Transverse CTE α	°C^{-1}	6.10E-06

The dimension of the sample can be seen in Fig. 1. The loading block was made from Al block and to adhere the loading block to the CFRP surface, the sandpaper P300 was applied from both of loading block surface and CFRP surface. Cyanoacrylate adhesive was applied in between surface to make excellent bonding during the loading process. Marked of the side part of the sample was used spray paint while the black mark was used sharp pencil in the designated distance followed the standard. The marks were set from the first 5 mm with duplication of marks every 1 mm. After that, the marking process continue every 5 mm until total marks were 25 mm as suggested from ASTM D 5528 [36] and ISO 15024 [32].

2.2. Methods

The testing process schematic can be seen in Fig. 2. The test followed the rules from ISO 15024 [32], which is also linked with ASTM D 5528 [36]. After the specimens were cut and cleaned for preparation, they were placed into the universal testing machine (UTM). The present study used the Zwick Roell Proline Z010 with a capacity load cell of 10 kN. The specimen was then applied with a constant loading rate of 2 mm/min. The specimens in the present study were divided into two categories: specimens with AE sensors adhered to the edge of the specimen, as shown in Fig. 2(a), and normal specimens without AE sensors. This condition was applied to determine the effect of the load that might be applied to the specimen due to the addition of AE sensors. The specimens were set so that the cracked edges touched each other, and the load was at zero load, as shown in Fig. 2(b). To investigate the crack length during the loading process, a loop or digital camera was used to take records and detect the crack in situ process until the test was completed (loading-unloading process finished), as shown in Fig. 2(c). During and after the test, data related to crack length (a), time (s), and the load (N) at each instance when the crack reached the predefined mark were collected.

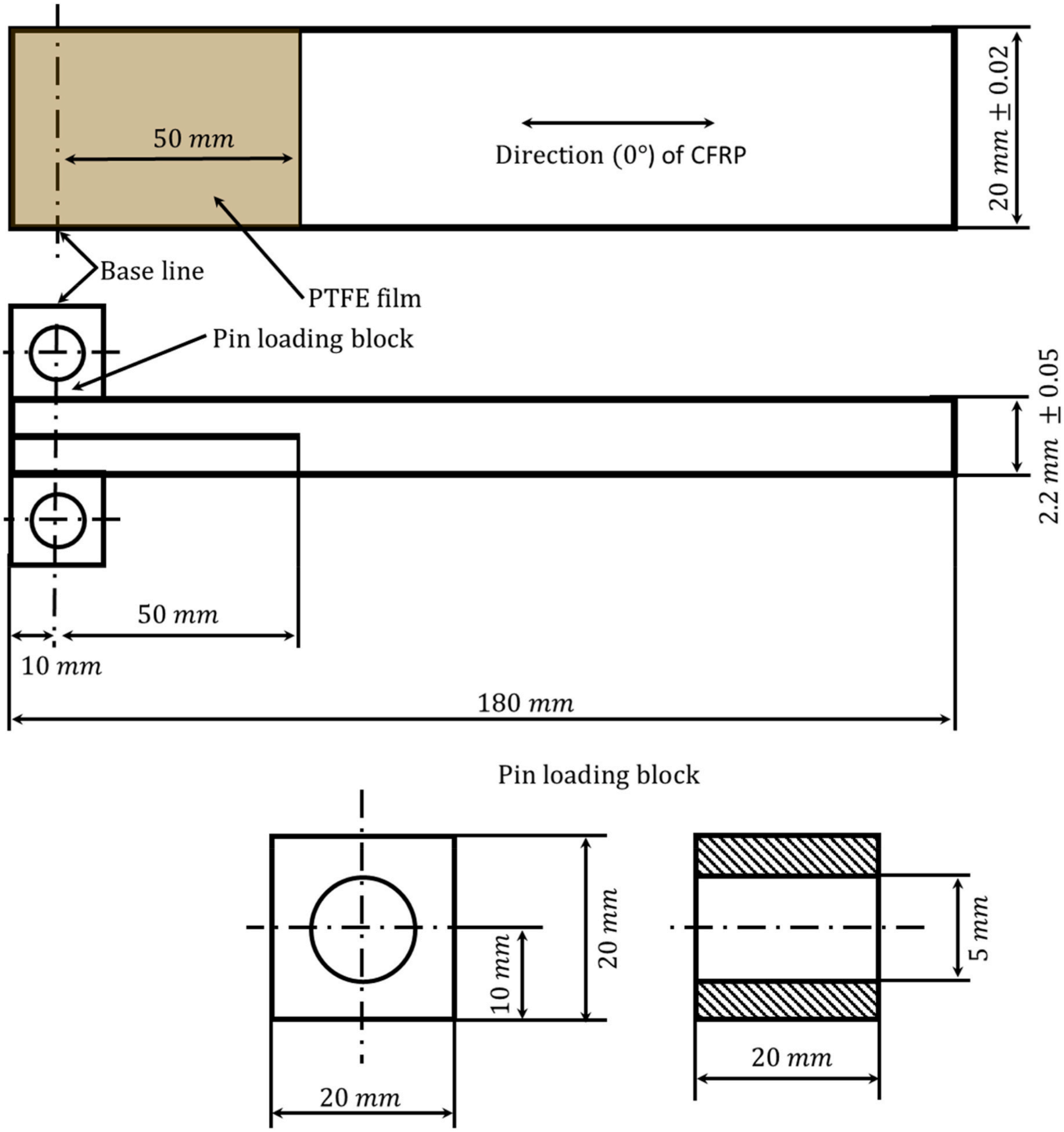

Fig. 1. Specimen dimension.

2.2.1. G_{IC} calculation methods

Calculation of G_{IC} in the present study was used 2 methods that described in the ISO 15024 [32]; Method A: Corrected beam theory (CBT), and Method B: Modified compliance calibration (MCC). These two methods were described in the following equations.

$$G_{IC}\ (CBT) = \frac{3P\delta}{2b(a+|\Delta|)} \times \frac{F}{N} \tag{1}$$

where G_{IC} was fracture toughness mode I (j/m^2); P was load (N); δ was displacement (mm); b was width of specimen (mm); a was total delamination length (mm); $|\Delta|$ was the extrapolation of a linear fit through the data in the plot yields Δ as the x-intercept; F was the large-displacement correction (described in Eq. (2)) (mm); and N was the load block correction (N).

$$F = 1 - \frac{3}{10}\left(\frac{\delta}{a}\right)^2 - \frac{2}{3}\left(\frac{\delta l_1}{a^2}\right) \tag{2}$$

$$N = 1 - \left(\frac{l_2}{a}\right)^3 - \frac{9}{8}\left[1 - \left(\frac{l_2}{a}\right)^2\right]\frac{\delta l_1}{a^2} - \frac{9}{35}\left(\frac{\delta}{a}\right)^2 \tag{3}$$

where l_1 was the distance from the center of the loading pin, or of the piano hinge axis, to the midplane of the specimen beam (mm); and l_2 was the distance from the loading-pin center to its edge (mm).

The G_{IC} that calculated from modified compliance calibration (MCC) can be seen in the following Eq. (4). It is shown that C was the displacement (δ) divided by Load (N) (mm/N).

$$G_{IC}\ (MCC) = \frac{3m}{2(2h)} \times \left(\frac{P}{b}\right)^2 \times \left(\frac{bC}{N}\right)^{\frac{2}{3}} \times F \tag{4}$$

2.2.2. Temperature effect

The DCB test samples was manufactured by using autoclave system that applied with high different temperature from room temperature to the curing periods (25 °C–180 °C). This thermal difference affects to the

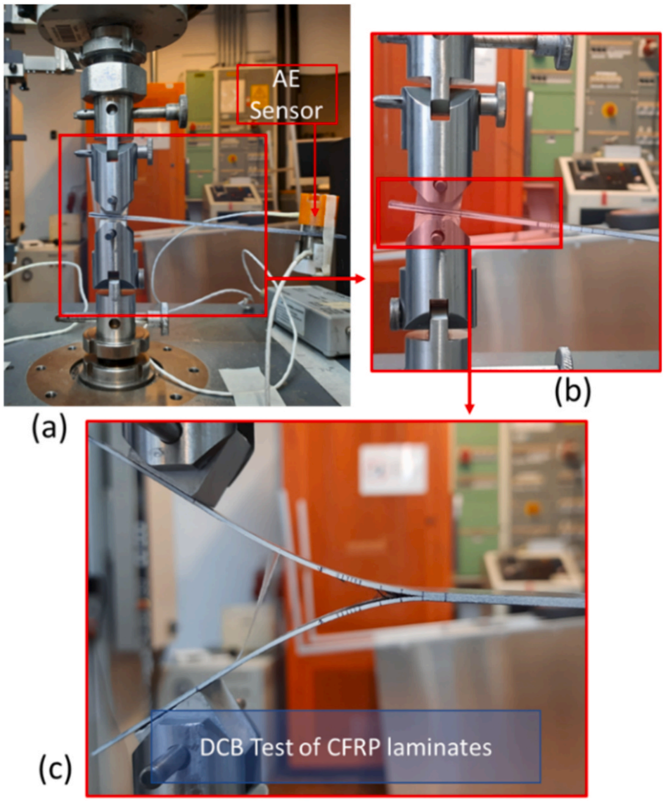

Fig. 2. Schematic of DCB Test where the AE sensor was adhered on the specimen.

Mode I. Previous study conducted by Muflikhun and Yokozeki [30] studied the temperature effect of the hybrid sample. The true fracture toughness [37] in Mode I can be calculated as follow:

$$G_I(DCB) = G_{DCB}^{exp.} + \frac{P\Delta T}{w}\left(\alpha_K^{(1)} - \alpha_K^{(2)}\right)a + \frac{(\Delta T)^2}{2w}\left(I^{(1)} + I^{(2)} - I^{(3)}\right) \tag{5}$$

Where ΔT is temperature different, $\alpha_K^{(k)} = \frac{A_{11}^{(k)}M_T^{(k)} - B_{11}^{(k)}N_T^{(k)}}{A_{11}^{(k)}D_{11}^{(k)} - B_{11}^{(k)2}}$, $I^{(k)} = N_T^{(k)}\alpha_\varepsilon^{(k)} + M_T^{(k)}\alpha_K^{(k)} - B\sum_i E_i^{(k)}\alpha_i^{(k)2}t_i^{(k)}$, and $t_i^{(k)}$ is the thickness of each layer.

Eq. (5) was generated from the theory of mechanics of composite materials as shown from the following Eq.;

$$\begin{bmatrix} \overline{N} \\ \overline{M} \end{bmatrix} = \begin{bmatrix} A & B \\ B & D \end{bmatrix} \begin{bmatrix} \varepsilon^\circ \\ \kappa \end{bmatrix} \tag{6}$$

$$\begin{bmatrix} \varepsilon^\circ \\ \kappa \end{bmatrix} = \begin{bmatrix} A' & B' \\ B' & D' \end{bmatrix} \begin{bmatrix} \overline{N} \\ \overline{M} \end{bmatrix} \tag{7}$$

$$\begin{bmatrix} N^{(k)} \\ M^{(k)} \end{bmatrix} = \begin{bmatrix} A_{11}^{(k)} & B_{11}^{(k)} \\ B_{11}^{(k)} & D_{11}^{(k)} \end{bmatrix} \begin{bmatrix} \varepsilon^{\circ(k)} \\ \kappa^{(k)} \end{bmatrix} - \begin{bmatrix} N_T^{(k)} \\ M_T^{(k)} \end{bmatrix} \Delta T \tag{8}$$

$$\begin{bmatrix} \varepsilon^{\circ(k)} \\ \kappa^{(k)} \end{bmatrix} = \begin{bmatrix} C_\varepsilon^{(k)} & D^{(k)} \\ D^{(k)} & C_\kappa^{(k)} \end{bmatrix} \begin{bmatrix} N^{(k)} \\ M^{(k)} \end{bmatrix} + \begin{bmatrix} \alpha_\varepsilon^{(k)} \\ \alpha_\kappa^{(k)} \end{bmatrix} \Delta T \tag{9}$$

The value of $A_{11}^{(k)}, B_{11}^{(k)}, D_{11}^{(k)}, N_T^{(k)}, M_T^{(k)}, C_\kappa^{(k)}, D^{(k)}, C_\varepsilon^{(k)}, \alpha_\kappa^{(k)}$, and $\alpha_\varepsilon^{(k)}$ can be determined by using Eqs. 10–17.

$$A_{11}^{(k)} = \sum_i^n (\overline{Q}_{11})_i \left(z_i^{(k)} - z_{i-1}^{(k)}\right) \tag{10}$$

$$B_{11}^{(k)} = \frac{1}{2}\sum_i^n (\overline{Q}_{11})_i \left(z_i^{(k)2} - z_{i-1}^{(k)2}\right) \tag{11}$$

$$D_{11}^{(k)} = \frac{1}{3}\sum_i^n (\overline{Q}_{11})_i \left(z_i^{(k)3} - z_{i-1}^{(k)3}\right) \tag{12}$$

$$N_T^{(k)} = A_{11}^{(k)}\alpha_i^{(k)} \tag{13}$$

$$M_T^{(k)} = B_{11}^{(k)}\alpha_i^{(k)} \tag{14}$$

$$C_\kappa^{(k)} = \frac{A_{11}^{(k)}}{A_{11}^{(k)}D_{11}^{(k)} - B_{11}^{(k)2}} \tag{15}$$

$$D^{(k)} = \frac{-B_{11}^{(k)2}}{A_{11}^{(k)}D_{11}^{(k)} - B_{11}^{(k)2}} \tag{16}$$

$$\alpha_\varepsilon^{(k)} = \frac{D_{11}^{(k)}N_T^{(k)} - B_{11}^{(k)}M_T^{(k)}}{A_{11}^{(k)}D_{11}^{(k)} - B_{11}^{(k)2}} \tag{17}$$

The flexural modulus of the laminates can be determined using Eq. (18).

$$E_f = \frac{8(a + |\Delta|)^3}{\frac{C}{N}bh^3} \tag{18}$$

E_f was flexural modulus (GPa).

3. Results and discussion

3.1. DCB load tests

The DCB test results gathered from UTM data can be seen in Fig. 3. The tests were classified with two categories, which are using AE devices and without AE devices. Since the AE sensors have initial weight that might affect to the results, the tests were set to evaluate this difference. Fig. 3 (a) showed the DCB test without AE sensors, and Fig. 3 (b) DCB test used AE sensors. The results showed that there is limited or no effect of the used of AE sensors on the load-displacement output. Thus, the AE sensors related to the weight that adhered on the specimen during the tests can be neglected. The tests showed that for the specimens [+45°/-45°/0°]$_{2S}$ have lower modulus but longer displacement compared to [0°/+45°/-45°]$_{2S}$ specimens. It is showed that the highest load of [+45°/-45°/0°]$_{2S}$ samples occurred around 23 N while for [0°/+45°/-45°]$_{2S}$ specimens occurred around 27 N. Another trend can be seen that [0°/+45°/-45°]$_{2S}$ have slightly drop after reached the certain load before it gains rebound load. This phenomenon has not seen for [+45°/-45°/0°]$_{2S}$ specimens where the inclination occurred longer and no indication of sudden drop before reach the final displacement that stated from the standard.

Data related DCB test that was plotted in Fig. 3, then being analyzed using the GIC calculation based on Eq. (1) to Eq. (4). The calculation was used 2 methods, CBT and MCC to be compared. For the CBT methods, the ΔCBT was calculated first and then plotted. The data used to determine the GIC as seen in Fig. 4 (a) and (c). Another method, MCC, are determine based on the m MCC plot. This data then used to determine the GIC as seen in Fig. 4 (b) and (d). Based on Fig. 4, the CBT and MCC method introduced from ISO 15024 [32] have similar trend to calculate the CFRP laminates. It is also shown that the used of AE sensor adhered on the surface of the specimen have less influenced to the performance of the test. It is mean that there is no impact or no significant impact to the test. Another trend showed that for [+45°/-45°/0°]$_{2S}$ specimens have lower GIC compared with [0°/+45°/-45°]$_{2S}$ specimens. This mean that the energy that needed for [+45°/-45°/0°]$_{2S}$ specimens to peeled fewer than [0°/+45°/-45°]$_{2S}$. Thus, the specimen

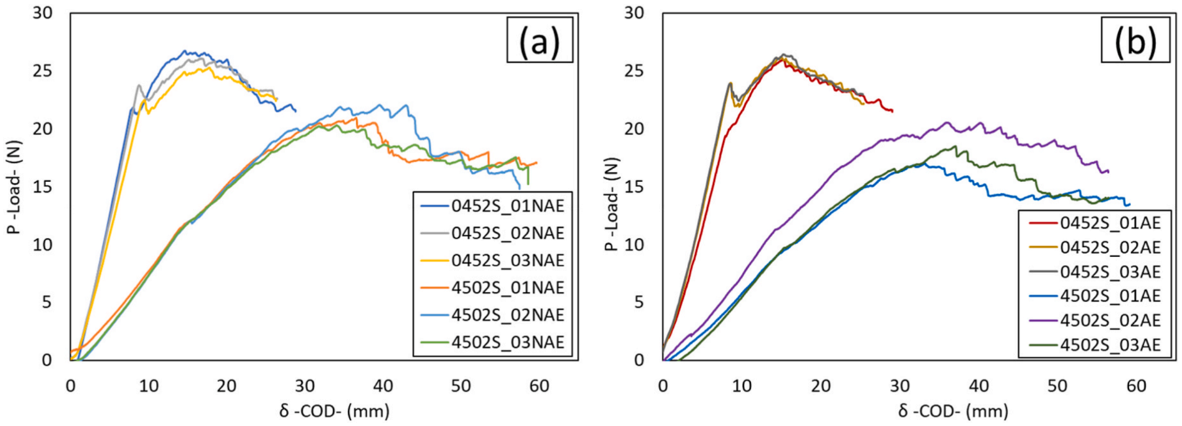

Fig. 3. Load-displacement curved from DCB tests, (a) Without AE sensors adhered, (b) With AE sensors adhered.

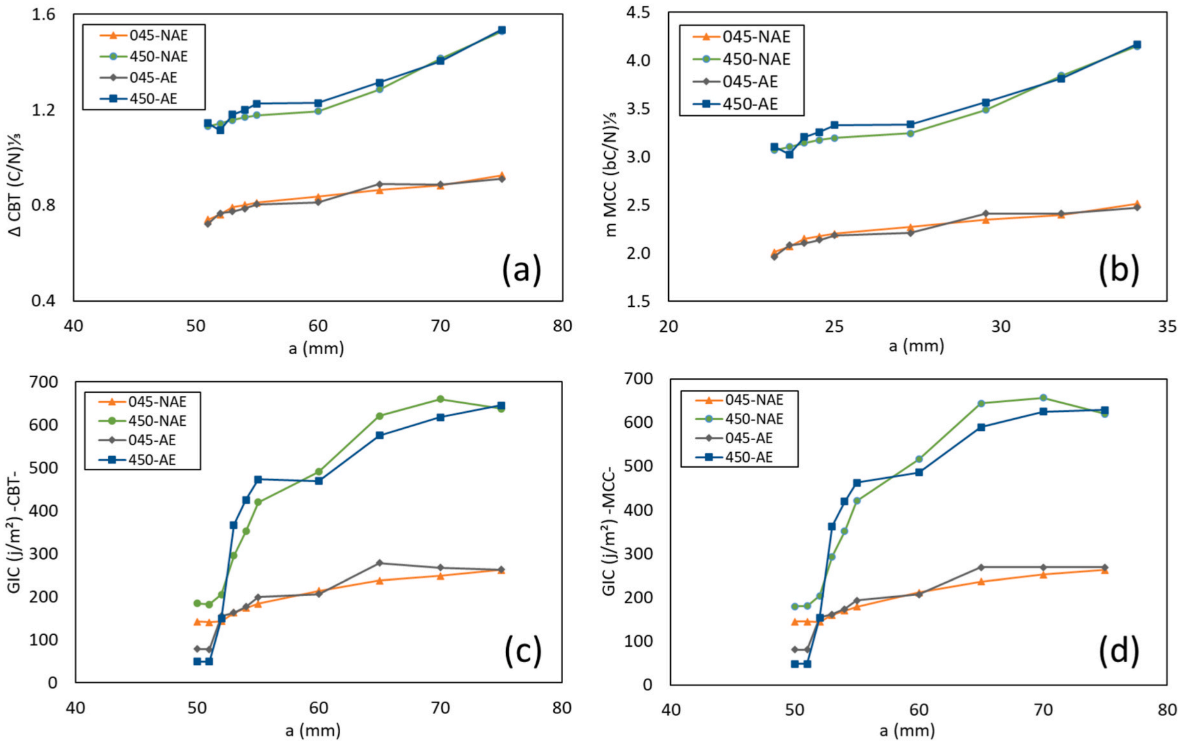

Fig. 4. GIC of all sample. (a) ΔCBT, (b) m MCC, (c) GIC CBT method, (d) GIC MCC method.

[0°/+45°/-45°]$_{2S}$ are tougher than [+45°/-45°/0°]$_{2S}$. However, by checking the load-displacement graphs, it is shown that the [+45°/-45°/0°]$_{2S}$ have longer displacement to withstand and maintaining its shape compared to [0°/+45°/-45°]$_{2S}$ specimen. Further analysis related to the modulus of the specimen are shown in Fig. 5.

The flexural modulus of all specimens can be seen in Fig. 5. It is shown that for [+45°/-45°/0°]$_{2S}$ laminates have lower flexural modulus with the average of 86.52 GPa and 91.94 GPa for non-acoustic emission (NAE) and AE specimens, compared with [0°/+45°/-45°]$_{2S}$ laminates with 927.7 GPa and 736.6 GPa for NAE and AE specimens, respectively. The modulus indicated that the resulting inclination caused by the loading gives different outcomes depending on the stacking sequences of the lamina. Higher the modulus indicated that the specimens could maintain its shape against the influence of loading in the direction of Mode I.

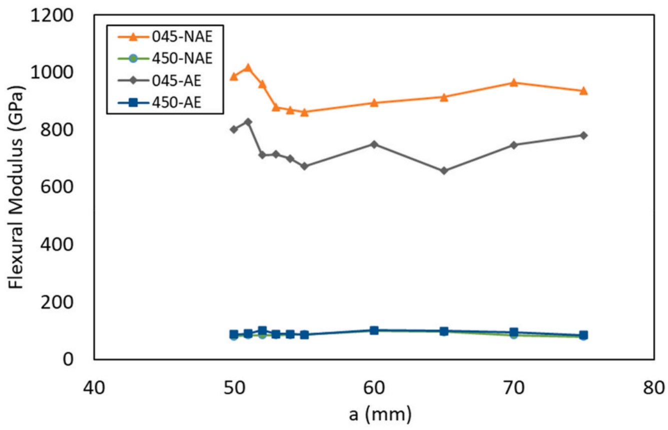

Fig. 5. Flexural modulus of representative samples.

3.2. Surface analysis and roughness evaluations

The present study conducts the micro structural analysis and roughness examinations of the specimen after being tested using Mode I loading. The Keyence VHX-7000 digital microscope was incorporated in the present study to acquired data for surface structure and roughness of the fractured specimens. These were presented by previous research on how the determination of surface roughness can give more comprehensive analysis related to the fractured specimens after tests [38,39].

From the microstructural evaluation of $[0°/+45°/-45°]_{2S}$ fractured specimen after DCB test, it is showed that the topology of the specimen has mirror shaped where the crack propagation occurred at the (−45°) layer in the middle of the laminates (Fig. 6(a and b)). The roughness of the surface also can be evaluated where in the perpendicular direction, the Ra revealed with 38 μm followed by (−45°) from the fiber direction with 43 μm as shown in Fig. 6. Layer delamination is shown in Fig. 6(a and b). This finding is visible when the naked eye is examined. Further, the 2D shape of the surface can be seen in Fig. 6(c and d). Both roughness topologies showed climbing as it ascended, indicating that some layers of CFRP have peeled off and adhered to other layers with a fracture path not precisely centered within the layers. The different elevations from the lowest to the highest reported up to 200 μm.

The surface conditions and the roughness topological for $[+45°/-45°/0°]_{2S}$ specimen are shown in Fig. 7. The macro scale of the fractured specimen is shown in Fig. 7 (a), where the detailed condition of the surface is shown in Fig. 7 (b) the surface showed that some of the layers are peeled and adhered on the other side. This condition is clarified from Fig. 7 (c and d) where the roughness of the specimen in early fractured area were examined. The peeled layer is not clearly as in the $[0°/+45°/-45°]_{2S}$ specimen indicate from the elevation and pattern of the roughness that mostly like hills and valleys and the height peak confirmed less than 100 μm.

3.3. Acoustic emission (AE)

The AE data from the present work were incorporated using the Micro-II Digital AE System by Physical Acoustics Corporation, Mistras, NJ, USA. The data were used to record the frequency that occurred during the Mode I loading, as shown in Fig. 8. For the complete data output references, all graphs are illustrated in Appendix (A1 and A2).

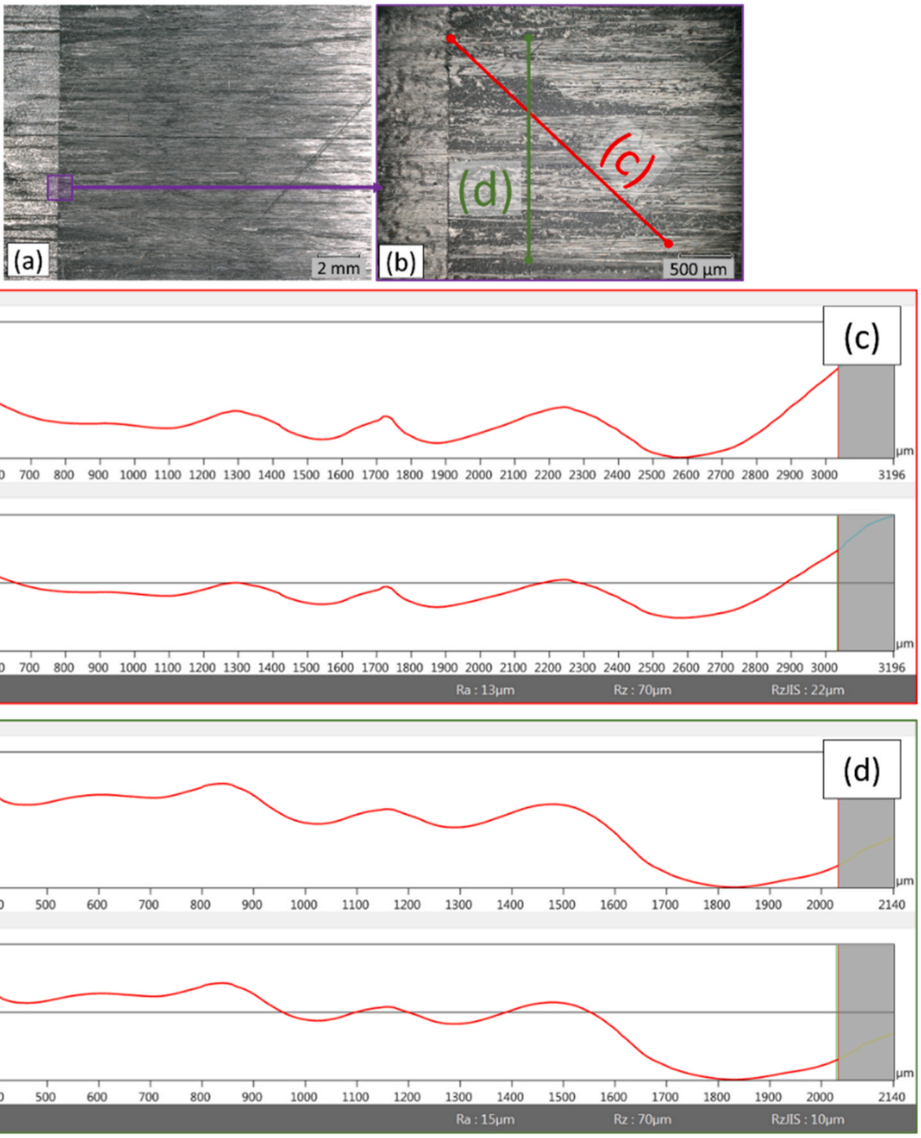

Fig. 6. Surface roughness and topography of the sample after DCB test for $[0°/+45°/-45°]_{2S}$ specimens. (a) macro scale from fractured specimen, (b) deeper scale of the barrier between PTFE film as the artificial cracked with the cracker specimen due to the loading process, (c) cross-sectional roughness of the surface, and (d) the longitudinal roughness of the surface.

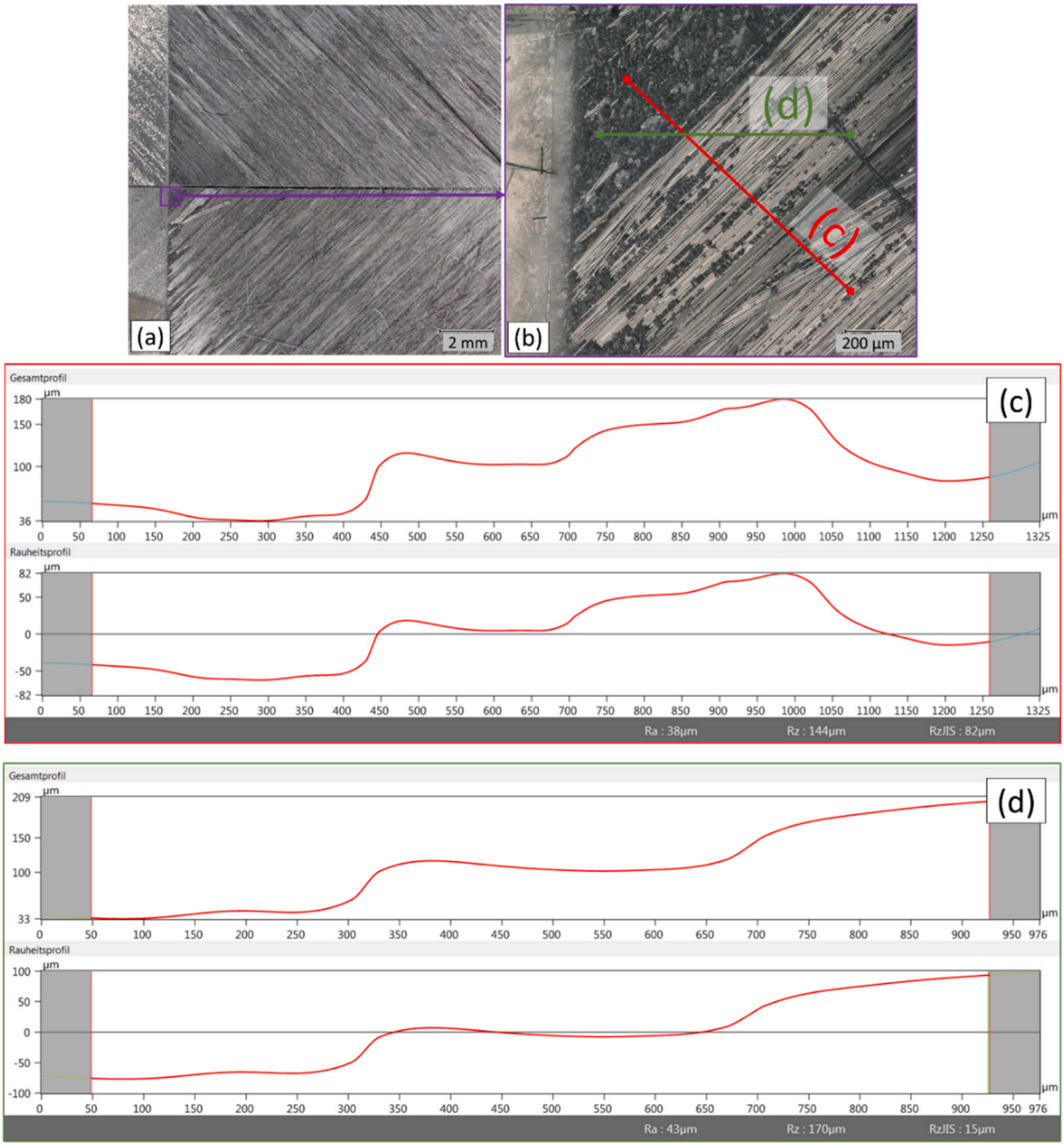

Fig. 7. Surface roughness and topography of the sample after DCB test for [+45°/-45°/0°]$_{2S}$. (a) macro scale from a fractured specimen, (b) deeper scale of the barrier between PTFE film as the artificial cracked with the cracker specimen due to the loading process, (c) 45° sectional roughness of the surface, and (d) the perpendicular roughness of the surface.

The comparison of the different laminates related to the number of hits between [0°/+45°/-45°]$_{2S}$ specimens and [+45°/-45°/0°]$_{2S}$ specimens is shown in Fig. 8(a and b), respectively. The results showed that the [+45°/-45°/0°]$_{2S}$ specimens have the ability to withstand more than twice the number of hits compared to the [0°/+45°/-45°]$_{2S}$ specimens, with more than 600 hits compared to less than 300 hits. The data were supported by the number of amplitude points from both types of specimens observed in Fig. 8(c and d), where the times that the [+45°/-45°/0°]$_{2S}$ specimens needed until final failure and the maximum amplitude recorded were 2.3 times longer and 23% higher than the [0°/+45°/-45°]$_{2S}$ specimens, respectively. The data were then compared related to the absolute energy culminated from the 2 different specimens, where the absolute energy of the [+45°/-45°/0°]$_{2S}$ specimens was recorded more than 10 times higher than the [0°/+45°/-45°]$_{2S}$ specimens.

The evaluation process using AE, which gathers data in real time during the testing period, is very important for understanding the failure pattern of the specimens. By using AE sensors, which can be recorded continuously in further applications in aerospace, engineers can detect and predict the quality of the structure precisely. It can also prevent catastrophic failure of the structure in cases where the application of destructive evaluation is impossible or impractical.

3.4. *Ultrasound analysis*

Non-destructive testing and analysis were also carried out in the present study. It was applied after specimen failure using the USPC 3040 DAC ultrasonic testing equipment from Hillger NDT GmbH, Brunswick, Germany. The evaluation used a distilled water bath flooded onto the specimen as the coupling medium. By employing a calibrated sound speed tailored to the plate’s thickness, the C-image displays variations in

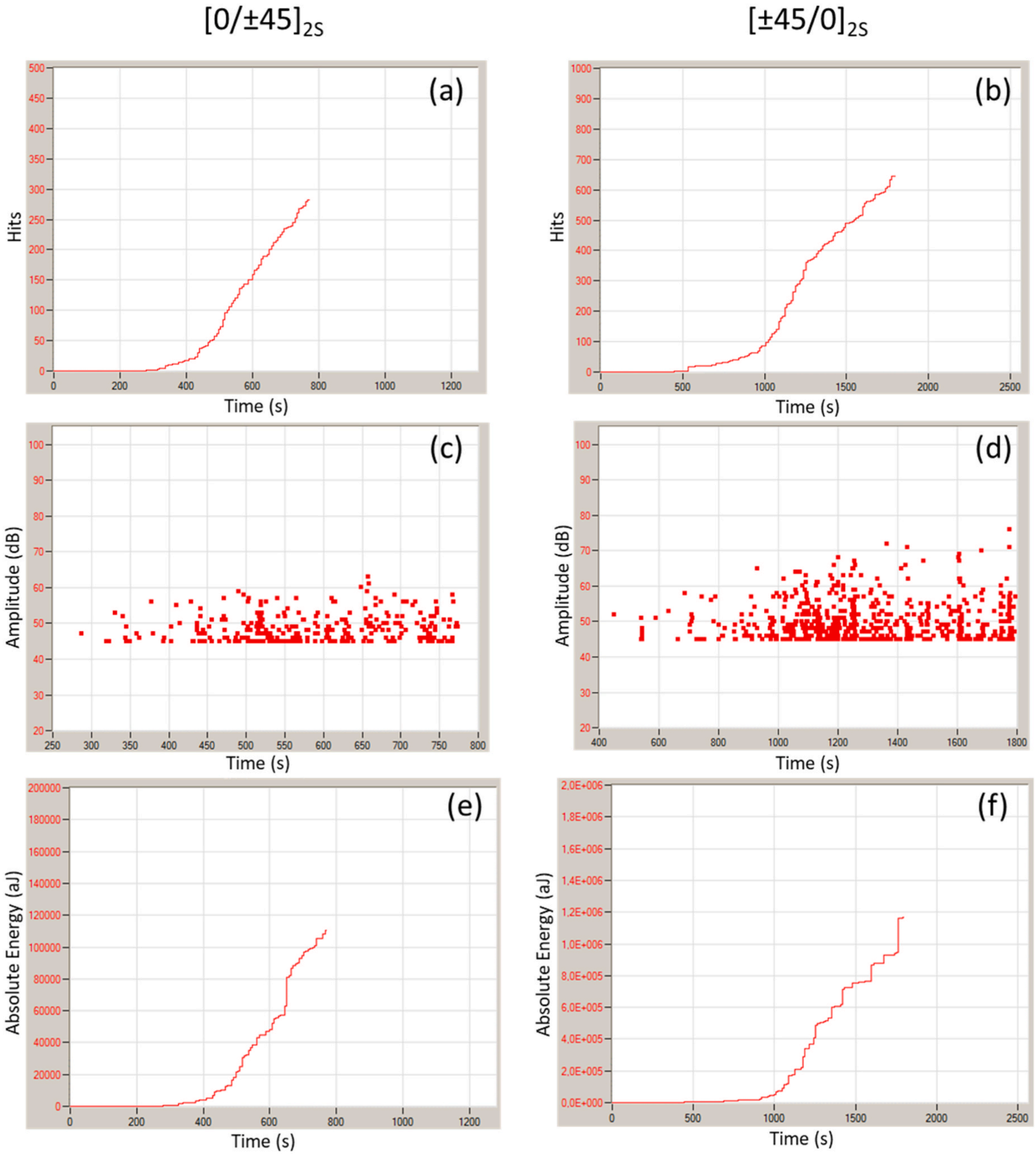

Fig. 8. AE data comparison between $[0°/+45°/\text{-}45°]_{2S}$ and $[+45°/\text{-}45°/0°]_{2S}$. (a) and (b) Hits vs Time, (c) and (d) Amplitude vs Time, and (e) and (f) Absolute energy vs Time.

plate thickness, enabling the characterization of changes in fiber content. Additionally, the C-image reveals the depth of defects, showcasing sites where fibers agglomerate.

The complete results from ultrasound analysis were listed in Appendix (A3-A4). The specific comparison related to the specimen after testing is shown in Fig. 9. The cracks and failure area in the $[+45°/\text{-}45°/0°]_{2S}$ specimen showed that the failure occurred with a higher frequency compared to the $[0°/+45°/\text{-}45°]_{2S}$ specimen. The ultrasound analysis also revealed that in terms of final failure related to the crack length, the $[0°/+45°/\text{-}45°]_{2S}$ specimen had a longer crack length compared to the $[+45°/\text{-}45°/0°]_{2S}$ specimen. This data, combined with AE analysis, revealed that in a shorter time, the crack in the $[0°/+45°/\text{-}45°]_{2S}$ specimen propagated faster than the $[+45°/\text{-}45°/0°]_{2S}$ specimen. Applying this to real applications, a faster crack propagation will reduce the lifetime and make the structure more dangerous.

3.5. *Thermal residual stress effect*

The manufacturing of composite materials is affected by different temperatures, where the coefficient of thermal expansion (CTE) applied can influence the structure or laminate system's actual performance. The present study applied theoretical calculations with different temperatures between room temperature and autoclave (manufacturing process) temperatures. We set the different temperatures in the range of 0, 10, 20, 30, 40, 50, 75, 100, 125, 150, 175, and 200 °C.

The calculation results, adopted from Eq. (5) and the values derived from Eq. (6) to Eq. (18), are shown in Fig. 10. The mode I critical energy release rate from the experimental testing and by comparing using MCC and MBT methods are demonstrated in Fig. 10 (a). The data showed that by adding AE sensors, there is a slight decrease in the GIC value, but it is not significant compared to the sample without using AE sensors.

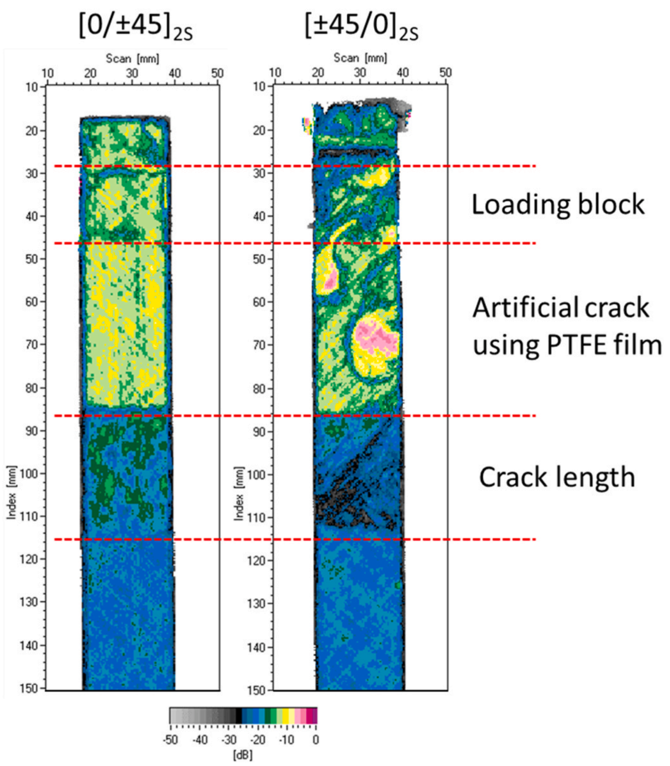

Fig. 9. Ultrasound image processing of DCB specimen ([+45°/-45°/0°]$_{2S}$ and [0°/+45°/-45°]$_{2S}$) after tests.

Further analysis using true fracture toughness (True GIC) is shown in Fig. 10 (b). By using the actual temperatures of the manufacturing process (room temperature 25 °C and autoclave temperature 180 °C), the calculation was made. Further analyses were conducted by using different temperatures to detect the ambience of the GIC values, as shown in Fig. 10 (c). The GIC values slightly changed and increased with the increase in the temperature difference. However, since the specimen manufactured was symmetric ([0°/+45°/-45°]2S and [+45°/-45°/0°]$_{2S}$), changes in the thermal residual stress did not significantly affect. The higher value of MCC method compared with CBT due to the equation that been used to determine the value of GIC. Further analysis and evaluation of composite laminates by using different sequences, incorporating advanced equipment, and using cost analysis were recommended to evaluate composite laminates in a more focused and precise study [40].

3.6. *Failure mechanism*

The present study showed that by using AE and ultrasound image processing, the failure mechanism can be used to detect the crack propagation of the laminates. The crack pattern form [0°/+45°/-45°]$_{2S}$ laminates have only 2 colors appear which are majority green and light green. This color indicate that the crack was in the same layer rather than occurred in interlayer. The color was more variety in [+45°/-45°/0°]$_{2S}$ laminates with green, black, and grey as seen in Fig. 11. The failure also shown that the crack timing for [0°/+45°/-45°]$_{2S}$ laminates much shorter (less than 800 s) than [+45°/-45°/0°]$_{2S}$ laminates (more than 1700 s). Another indication also can be seen in Fig. 11 where the delamination length for [0°/+45°/-45°]$_{2S}$ laminates much shorter (around 25 mm) than [+45°/-45°/0°]$_{2S}$ laminates (more than 50 mm). This indication showed that the failure mechanism of the laminates was majority affected by the angle of the layers where the delamination was

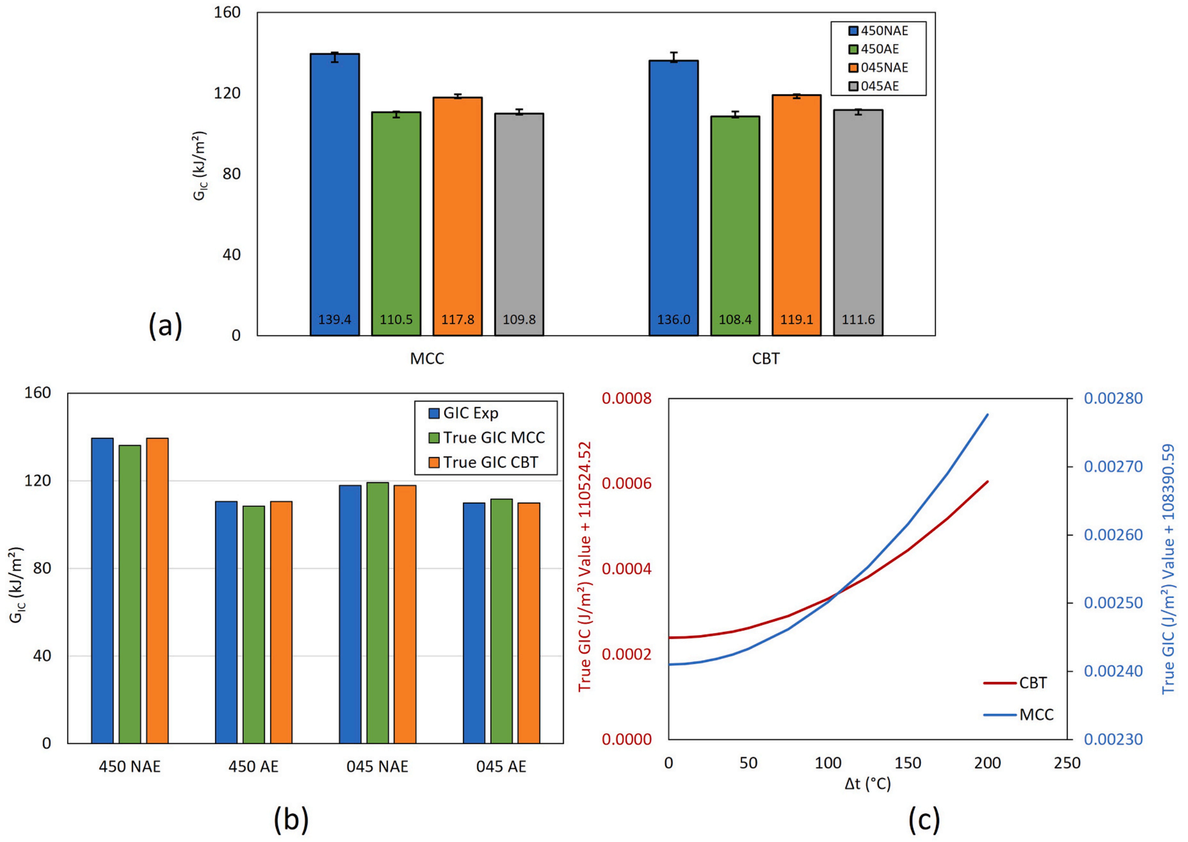

Fig. 10. (a) G_{IC} results from all specimens, (b) True fracture toughness (G_{IC}), (c) The effect of temperature in manufacturing process related to the G_{IC}.

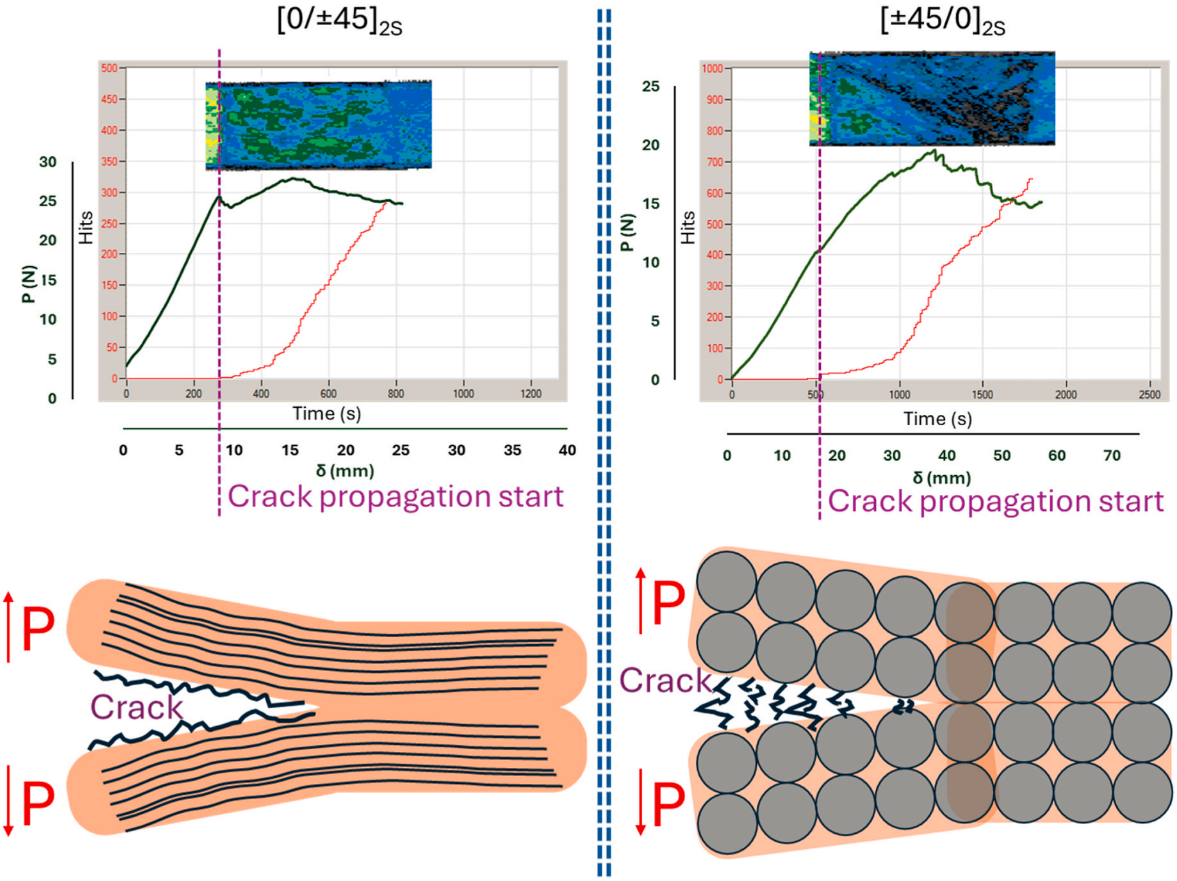

Fig. 11. The failure mechanism tracked by using experimental loading, AE, and ultrasound analysis of $[0°/+45°/-45°]_{2S}$ and $[+45°/-45°/0°]_{2S}$ laminates. Dark green line is the load-displacement data, red line was AE data, and the color figure was the ultrasound images.

occurred. The 0° layers exhibited crack growth faster than 45° layers. This occurred due to the angle effect of the lamina. The crack growth can be delayed when the fiber was cross sectional to the crack direction as shown in Fig. 11 for $[+45°/-45°/0°]_{2S}$ laminates. The other side, the fast crack growth detected in $[0°/+45°/-45°]_{2S}$ laminates due to the fiber orientation was align with the crack direction.

4. Conclusion

The present study successfully conducted a comprehensive analysis of CFRP laminates using real-time non-destructive testing (NDT) and post-testing. The Mode I (DCB Test) loading was incorporated, and two different laminates ($[0°/+45°/-45°]_{2S}$ and $[+45°/-45°/0°]_{2S}$) were applied for comparison. The results showed that by applying AE sensors, early failure in the laminates can be predicted and reported. The $[+45°/-45°/0°]_{2S}$ specimen demonstrated superior durability, lasting twice as long to failure compared to the $[0°/+45°/-45°]_{2S}$ specimen as reported in AE. Further characterization using calculations based on ISO 15024 and ASTM D5528 also showed a similar pattern. After the specimens were tested, ultrasound analysis revealed that the $[0°/+45°/-45°]_{2S}$ specimen not only failed faster compared to the $[+45°/-45°/0°]_{2S}$ specimen but also indicated a longer crack length. These results can raise awareness among engineers and researchers on how to choose the proper and correct laminates, where not only strength can be achieved but also durability to prevent crack propagations. In the present sequences, by applying the $[+45°/-45°/0°]_{2S}$ laminate in several applications such as aerospace and aircraft structures, researchers can predict a longer lifetime for the structure, reduce waste materials, and prevent more significant emissions from the manufacturing process.

Declaration of competing interest

The authors declare that they have no known competing financial interests or personal relationships that could have appeared to influence the work reported in this paper.

Acknowledgment

The authors want to thank Dr. Hans Wittich, Dr.-Ing. Dennis Gibhardt, Janina Mittelhaus, Tobias Tiedemann, and Christina Buggisch for the assistance during experimental analysis.

Appendix

A1-A2. Acoustic emission (AE) data.
A3-A4. Ultrasound data scanning.

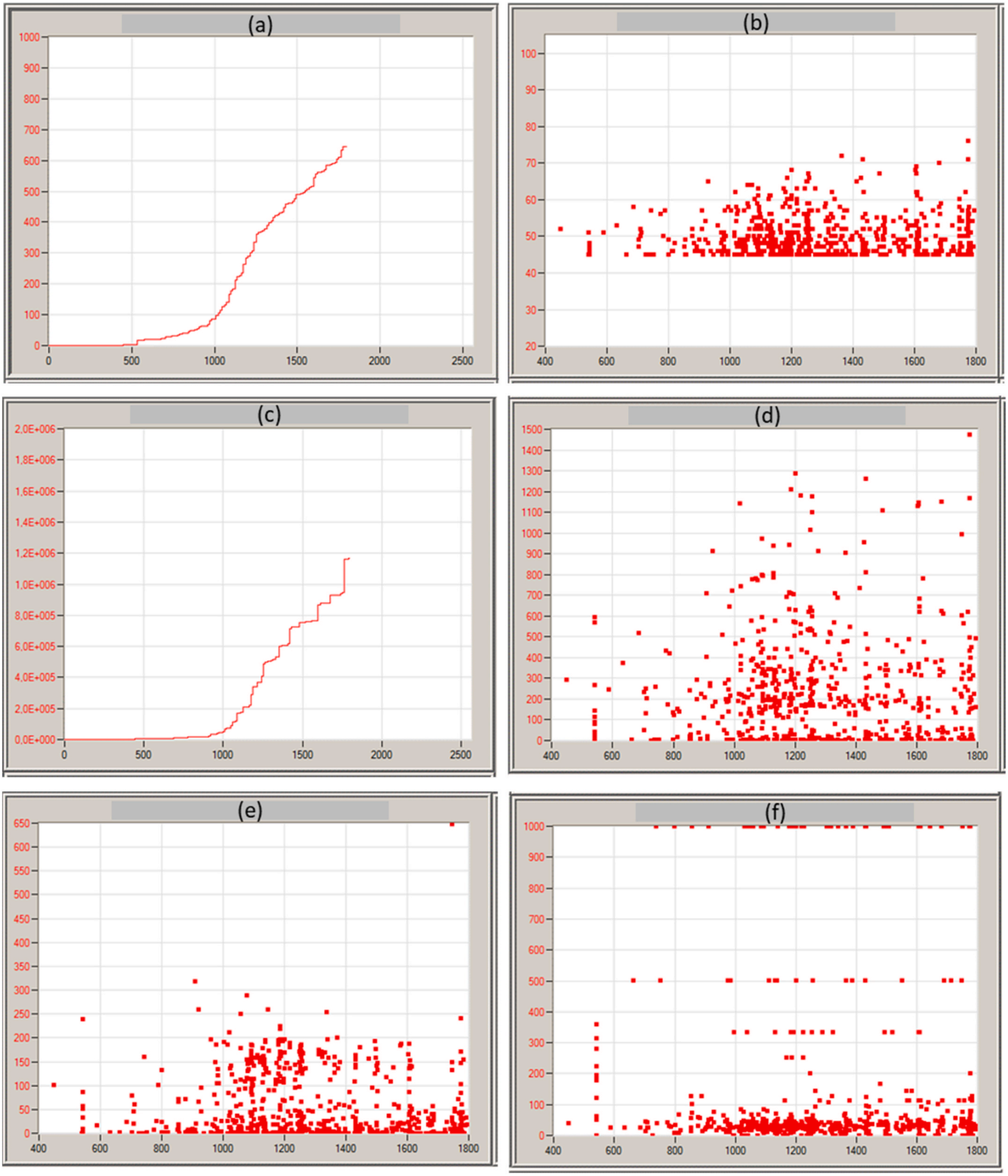

Fig. A1. Acoustic emission data for [+45°/-45°/0°]$_{2S}$. (a) Hits vs Time (s), (b) Amplitude (dB) vs Time (s), (c) Absolute Energy (aJ) vs Time (s), (d) Duration (μs) vs Time (s), (e) Rise time (μs) vs Time (s), (f) Ave. Freq. (kHz) vs Time (s).

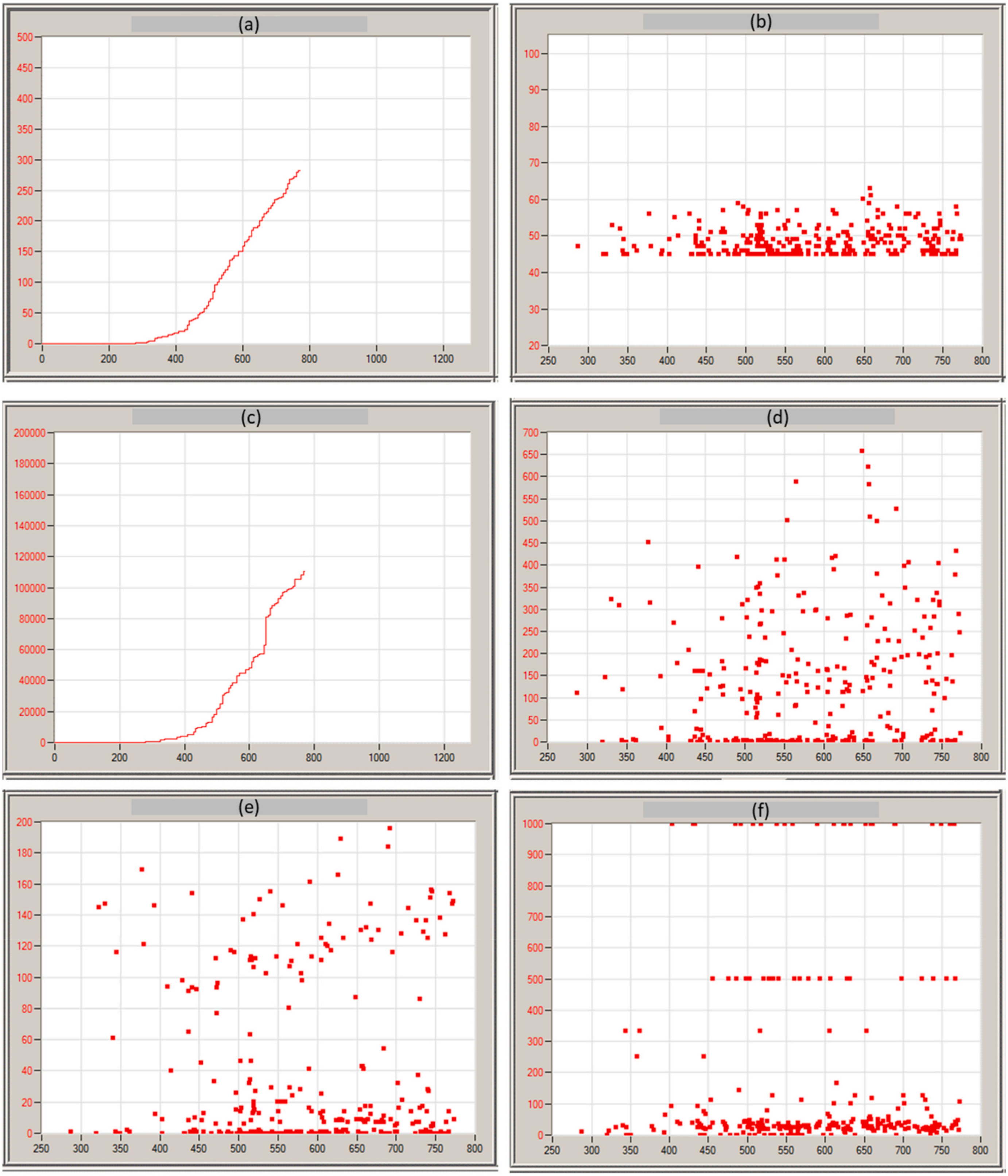

Fig. A2. AE data for $[0^\circ/+45^\circ/-45^\circ]_{2S}$. (a) Hits vs Time (s), (b) Amplitude (dB) vs Time (s), (c) Absolute Energy (aJ) vs Time (s), (d) Duration (μs) vs Time (s), (e) Rise time (μs) vs Time (s), (f) Ave. Freq. (kHz) vs Time (s).

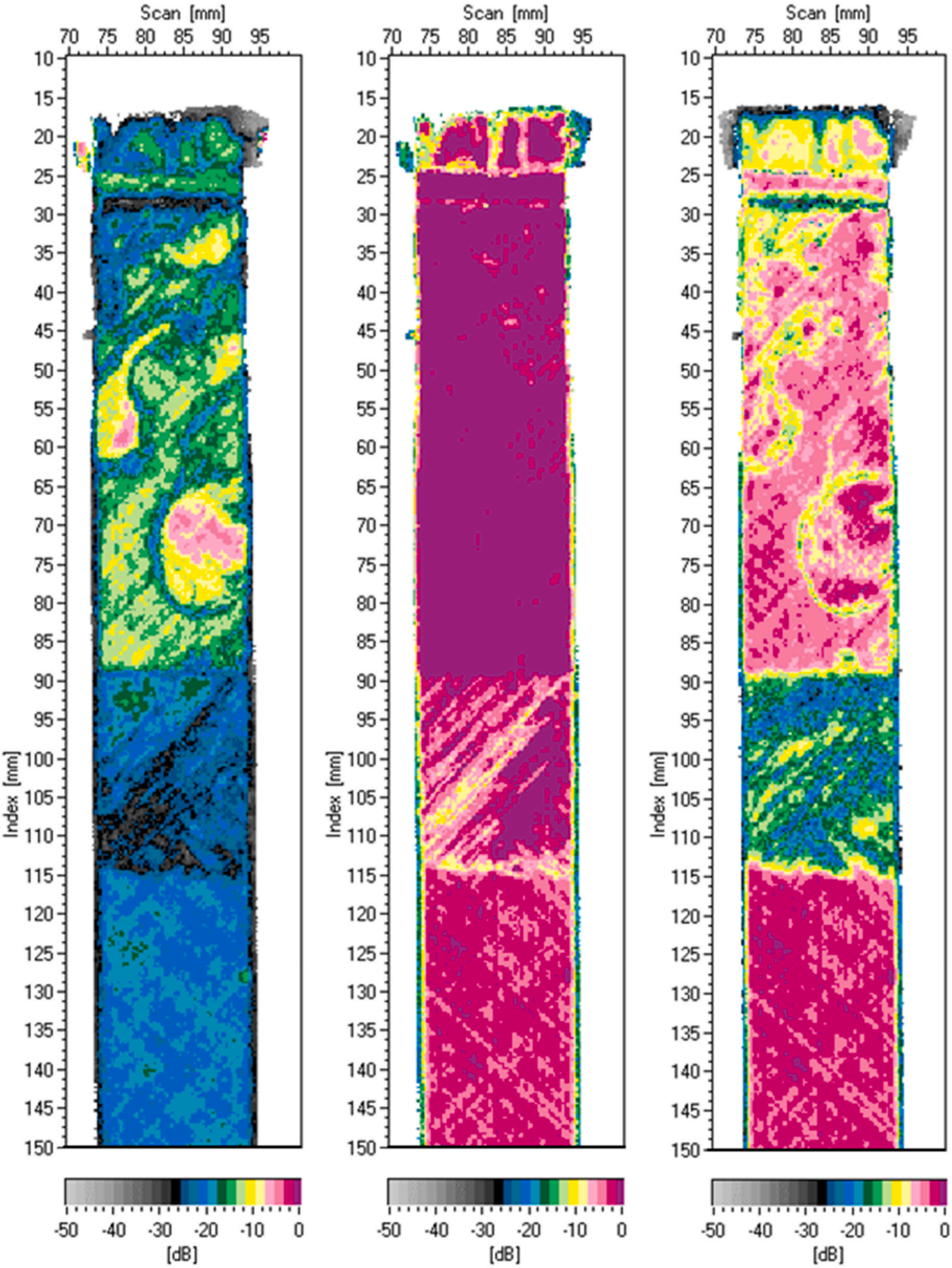

Fig. A3. Ultrasound image processing of DCB specimen ([+45°/-45°/0°]$_{2S}$) after tests.

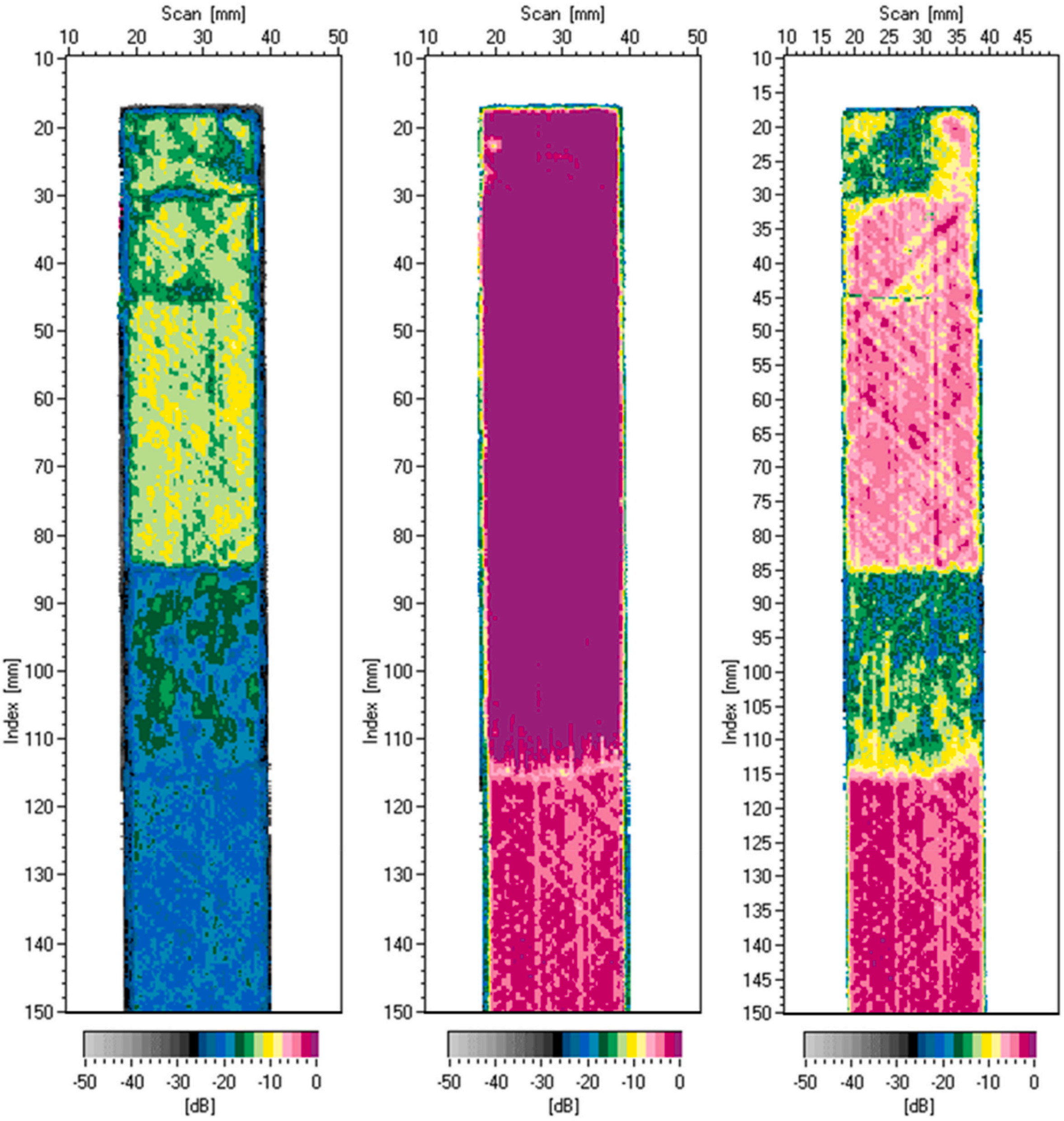

Fig. A4. Ultrasound image processing of DCB specimen ([0°/+45°/-45°]$_{2S}$) after tests.

References

[1] Li C, Ke L, He J, Chen Z, Jiao Y. Effects of mechanical properties of adhesive and CFRP on the bond behavior in CFRP-strengthened steel structures. Compos Struct 2018;211:163–74. https://doi.org/10.1016/J.COMPSTRUCT.2018.12.020.

[2] Séguin-Charbonneau L, Walter J, Théroux LD, Scheed L, Beausoleil A, Masson B. Automated defect detection for ultrasonic inspection of CFRP aircraft components. NDT E Int 2021;122. https://doi.org/10.1016/j.ndteint.2021.102478.

[3] Naito M, Kitamura H, Koike M, Kusano H, Kusumoto T, Uchihori Y, et al. Applicability of composite materials for space radiation shielding of spacecraft. Life Sci Space Res 2021;31:71–9. https://doi.org/10.1016/j.lssr.2021.08.004.

[4] Shao W, Sun Q, Xu X, Yue W, Shi D. Durability life prediction and horizontal bearing characteristics of CFRP composite piles in marine environments. Constr Build Mater 2023;367. https://doi.org/10.1016/j.conbuildmat.2022.130116.

[5] Muflikhun MA, Yokozeki T, Aoki T. The strain performance of thin CFRP-SPCC hybrid laminates for automobile structures. Compos Struct 2019;220:11–8. https://doi.org/10.1016/j.compstruct.2019.03.094.

[6] Chua CYX, Liu HC, Di Trani N, Susnjar A, Ho J, Scorrano G, et al. Carbon fiber reinforced polymers for implantable medical devices. Biomaterials 2021;271. https://doi.org/10.1016/j.biomaterials.2021.120719.

[7] Muflikhun MA, Yokozeki T. Systematic analysis of fractured specimens of composite laminates: different perspectives between tensile, flexural, Mode I, and Mode II test. International Journal of Int. j. Lightweight. Mater. Manufact. 2023;6. https://doi.org/10.1016/j.ijlmm.2023.03.003.

[8] Jiang H, Ji Y, Hu Y, Hu X, Ren Y. Interfacial design and flexural property of CFRP/aluminum-honeycomb sandwich with Aramid-pulp micro/nano-fiber interlays. Compos Struct 2022;289. https://doi.org/10.1016/j.compstruct.2022.115486.

[9] James S, Dang C. Investigation of shear failure load in ultrasonic additive manufacturing of 3D CFRP/Ti structures. J Manuf Process 2020;56:1317–21. https://doi.org/10.1016/j.jmapro.2020.04.026.

[10] Basha M, Wagih A, Melaibari A, Lubineau G, Abdraboh AM, Eltaher MA. Impact and post-impact response of lightweight CFRP/wood sandwich composites. Compos Struct 2022;279. https://doi.org/10.1016/j.compstruct.2021.114766.

[11] Zhang J, Lin G, Vaidya U, Wang H. Past, present and future prospective of global carbon fibre composite developments and applications. Compos B Eng 2023;250. https://doi.org/10.1016/j.compositesb.2022.110463.

[12] Carrasco-Baltasar D, García-Castillo S, Ivañez I, Navarro C. Modelling of woven CFRP plates subjected to oblique high-velocity impact and membrane loads. Compos Struct 2023;303. https://doi.org/10.1016/j.compstruct.2022.116344.

[13] Tao N, Anisimov AG, Groves RM. Shearography non-destructive testing of thick GFRP laminates: numerical and experimental study on defect detection with

thermal loading. Compos Struct 2022;282. https://doi.org/10.1016/j.compstruct.2021.115008.
[14] Bull PH, Edgren F. Compressive strength after impact of CFRP-foam core sandwich panels in marine applications. Compos B Eng 2004;35:535–41. https://doi.org/10.1016/j.compositesb.2003.11.007.
[15] Daynes S, Weaver P. Analysis of unsymmetric CFRP-metal hybrid laminates for use in adaptive structures. Compos Part A Appl Sci Manuf 2010;41:1712–8. https://doi.org/10.1016/j.compositesa.2010.08.009.
[16] Nugraha AD, Alandro D, Mangunkusumo KGH, Kusni M, Wu YC, Muflikhun MA. Failure configuration and evaluation of hybrid CFRP-GFRP laminates using innovative Arcan fixture: experimental and simulation approach. Composites Part C: Open Access 2024;14:100452. https://doi.org/10.1016/j.jcomc.2024.100452.
[17] Wang M, He M, Liang Z, Wu D, Wang Y, Qing X, et al. Fatigue damage monitoring of composite laminates based on acoustic emission and digital image correlation techniques. Compos Struct 2023;321. https://doi.org/10.1016/j.compstruct.2023.117239.
[18] Golewski P, Sadowski T, Kneć M, Budka M. The effect of thermal aging degradation of CFRP composite on its mechanical properties using destructive and non-destructive methods and the DIC system. Polym Test 2023;118. https://doi.org/10.1016/j.polymertesting.2022.107902.
[19] Mirzaei AH, Shokrieh MM. Evolution of the temperature rise and damage in laminated composites with stress concentration under fatigue loading. Compos B Eng 2023;254. https://doi.org/10.1016/j.compositesb.2023.110607.
[20] Yang X, Ju B feng, Kersemans M. Ultrasonic tomographic reconstruction of local fiber orientation in multi-layer composites using Gabor filter-based information diagram method. NDT E Int 2021;124. https://doi.org/10.1016/j.ndteint.2021.102545.
[21] Boursier Niutta C, Tridello A, Belingardi G, Paolino DS. Nondestructive determination of local material properties of laminated composites with the impulse excitation technique. Compos Struct 2021;262. https://doi.org/10.1016/j.compstruct.2021.113607.
[22] Kidangan RT, Krishnamurthy CV, Balasubramaniam K. Identification of the fiber breakage orientation in carbon fiber reinforced polymer composites using induction thermography. NDT E Int 2021;122. https://doi.org/10.1016/j.ndteint.2021.102498.
[23] Palumbo D, De Finis R, Galietti U. Thermoelastic stress analysis as a method for the quantitative non-destructive evaluation of bonded CFRP T-joints. NDT E Int 2021;124. https://doi.org/10.1016/j.ndteint.2021.102526.
[24] Pedrayes OD, Lema DG, Usamentiaga R, Venegas P, García DF. Semantic segmentation for non-destructive testing with step-heating thermography for composite laminates. Measurement 2022;200. https://doi.org/10.1016/j.measurement.2022.111653.
[25] Ardebili A, Alaei MH. Non-destructive testing of delamination defects in GFRP patches using step heating thermography. NDT E Int 2022;128. https://doi.org/10.1016/j.ndteint.2022.102617.
[26] Gahleitner L, Thummerer G, Reitinger B, Meirer K, Mayr G. 3D photothermal reconstruction of subsurface defects in notched multidirectional CFRP laminates due to tensile fatigue loading. NDT E Int 2022;131. https://doi.org/10.1016/j.ndteint.2022.102702.
[27] Kim HS, Park DW, Kim S Il, Oh GH, Kim HS. Non-destructive detection of thin micro-defects in glass reinforced polymer composites using a terahertz electro–magnetic wave based on a convolution neural network. Compos B Eng 2023;257. https://doi.org/10.1016/j.compositesb.2023.110694.
[28] Nastos C, Komninos P, Zarouchas D. Non-destructive strength prediction of composite laminates utilizing deep learning and the stochastic finite element methods. Compos Struct 2023;311. https://doi.org/10.1016/j.compstruct.2023.116815.
[29] Iwahori Y, Nakane K, Watanabe N. DCB test simulation of stitched CFRP laminates using interlaminar tension test results. Compos Sci Technol 2009;69:2315–22. https://doi.org/10.1016/j.compscitech.2008.12.018.
[30] Muflikhun MA, Yokozeki T. Steel plate cold commercial - carbon fiber reinforce plastics hybrid laminates for automotive applications: curing perspective with thermal residual effect. J Mater Res Technol 2021;14:2700–14. https://doi.org/10.1016/j.jmrt.2021.07.152.
[31] Zhou J, Huang ZM, Xu W. Prediction of laminate delamination from strength failure of interlaminar matrix-layer. J Reinforc Plast Compos 2023;42:177–87. https://doi.org/10.1177/07316844221105289.
[32] ISO-15024 Fibre-reinforced plastic composites-Determination of mode I interlaminar fracture toughness, G IC , for unidirectionally reinforced materials. 2023.
[33] HexPly ® M21. 2020.
[34] Psarras S, Muñoz R, Ghajari M. Compression performance of composite plates after multi-site impacts: a combined experimental and finite element study. Compos Struct 2023;322. https://doi.org/10.1016/j.compstruct.2023.117342.
[35] Wan L, Ismail Y, Sheng Y, Wu K, Yang D. Progressive failure analysis of CFRP composite laminates under uniaxial tension using a discrete element method. J Compos Mater 2021;55:1091–108. https://doi.org/10.1177/0021998320961460.
[36] ASTM D 5528 - 13. Standard test method for mode I interlaminar fracture toughness of unidirectional fiber-reinforced polymer matrix composites. ASTM International, n.d, p. 1–12.
[37] Yokozeki T, Ogasawara T, Aoki T. Correction method for evaluation of interfacial fracture toughness of DCB, ENF and MMB specimens with residual thermal stresses. Compos Sci Technol 2008;68:760–7. https://doi.org/10.1016/j.compscitech.2007.08.025.
[38] Muflikhun MA, Fiedler B. Failure prediction and surface characterization of GFRP laminates: a study of stepwise loading. Polymers 2022;14. https://doi.org/10.3390/polym14204322.
[39] Nugraha AD, Syahril M, Muflikhun MA. Excellent performance of hybrid model manufactured via additive manufacturing process reinforced with GFRP for sport climbing equipment. Heliyon 2023;9:e14706. https://doi.org/10.1016/j.heliyon.2023.e14706.
[40] Muflikhun MA, Yokozeki T. Experimental and numerical analysis of CFRP-SPCC hybrid laminates for automotive and structural applications with cost analysis assessment. Compos Struct 2021;263:113707. https://doi.org/10.1016/j.compstruct.2021.113707.